



**HAL**  
open science

## **Bi<sub>2</sub>(C<sub>2</sub>O<sub>4</sub>)<sub>3</sub>×7H<sub>2</sub>O and Bi(C<sub>2</sub>O<sub>4</sub>)OH Oxalates Thermal Decomposition Revisited. Formation of Nanoparticles with a Lower Melting Point than Bulk Bismuth**

Pierre Roumanille, Valérie Baco-Carles, Corine Bonningue, Michel Gougeon, Benjamin Duployer, Philippe Monfraix, Hoa Le Trong, Philippe Tailhades

### ► To cite this version:

Pierre Roumanille, Valérie Baco-Carles, Corine Bonningue, Michel Gougeon, Benjamin Duployer, et al.. Bi<sub>2</sub>(C<sub>2</sub>O<sub>4</sub>)<sub>3</sub>×7H<sub>2</sub>O and Bi(C<sub>2</sub>O<sub>4</sub>)OH Oxalates Thermal Decomposition Revisited. Formation of Nanoparticles with a Lower Melting Point than Bulk Bismuth. *Inorganic Chemistry*, 2017, 56 (16), pp.9486-9496. 10.1021/acs.inorgchem.7b00608 . hal-02009024

**HAL Id: hal-02009024**

**<https://hal.science/hal-02009024>**

Submitted on 6 Feb 2019

**HAL** is a multi-disciplinary open access archive for the deposit and dissemination of scientific research documents, whether they are published or not. The documents may come from teaching and research institutions in France or abroad, or from public or private research centers.

L'archive ouverte pluridisciplinaire **HAL**, est destinée au dépôt et à la diffusion de documents scientifiques de niveau recherche, publiés ou non, émanant des établissements d'enseignement et de recherche français ou étrangers, des laboratoires publics ou privés.



## Open Archive Toulouse Archive Ouverte (OATAO)

OATAO is an open access repository that collects the work of Toulouse researchers and makes it freely available over the web where possible

This is an author's version published in: <http://oatao.univ-toulouse.fr/19794>

**Official URL:** <https://doi.org/10.1021/acs.inorgchem.7b00608>

### To cite this version:

Roumanille, Pierre<sup>ORCID</sup> and Baco-Carles, Valérie<sup>ORCID</sup> and Bonningue, Corine<sup>ORCID</sup> and Gougeon, Michel<sup>ORCID</sup> and Duployer, Benjamin<sup>ORCID</sup> and Monfraix, Philippe and Le Trong, Hoa and Tailhades, Philippe<sup>ORCID</sup> *Bi<sub>2</sub>(C<sub>2</sub>O<sub>4</sub>)<sub>3</sub>·7H<sub>2</sub>O and Bi(C<sub>2</sub>O<sub>4</sub>)OH Oxalates Thermal Decomposition Revisited. Formation of Nanoparticles with a Lower Melting Point than Bulk Bismuth.* (2017) *Inorganic Chemistry*, 56 (16). 9486-9496. ISSN 0020-1669

Any correspondence concerning this service should be sent to the repository administrator: [tech-oatao@listes-diff.inp-toulouse.fr](mailto:tech-oatao@listes-diff.inp-toulouse.fr)

# Bi<sub>2</sub>(C<sub>2</sub>O<sub>4</sub>)<sub>3</sub>·7H<sub>2</sub>O and Bi(C<sub>2</sub>O<sub>4</sub>)OH Oxalates Thermal Decomposition Revisited. Formation of Nanoparticles with a Lower Melting Point than Bulk Bismuth

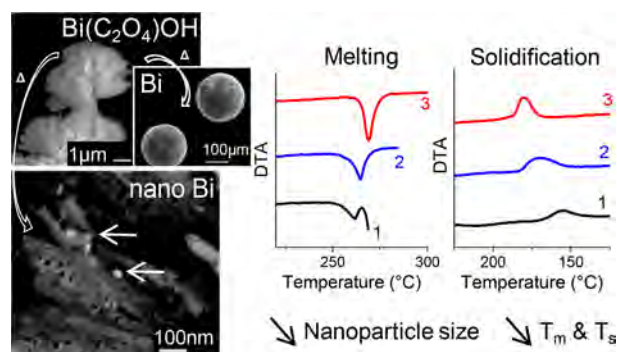
Pierre Roumanille,<sup>\*,†,‡,§</sup> Valérie Baco-Carles,<sup>‡</sup> Corine Bonningue,<sup>‡</sup> Michel Gougeon,<sup>‡</sup> Benjamin Duployer,<sup>‡</sup> Philippe Monfraix,<sup>†</sup> Hoa Le Trong,<sup>†</sup> and Philippe Tailhades<sup>‡</sup>

<sup>†</sup>Institut de Recherche Technologique Saint Exupéry, 118 route de Narbonne, CS 44248, 31432 Toulouse Cedex 4, France

<sup>‡</sup>Institut Carnot Chimie Balard Cirimat, UMR CNRS 5085, Université de Toulouse, CNRS, INPT, UPS, Université Toulouse 3 Paul Sabatier, 118 route de Narbonne, 31062 Toulouse Cedex 9, France

## Supporting Information

**ABSTRACT:** Two bismuth oxalates, namely, Bi<sub>2</sub>(C<sub>2</sub>O<sub>4</sub>)<sub>3</sub>·7H<sub>2</sub>O and Bi(C<sub>2</sub>O<sub>4</sub>)OH, were studied in terms of synthesis, structural characterization, particle morphology, and thermal behavior under several atmospheres. The oxalate powders were produced by chemical precipitation from bismuth nitrate and oxalic acid solutions under controlled pH, then characterized by X-ray diffraction (XRD), temperature-dependent XRD, IR spectroscopy, scanning electron microscopy, and thermogravimetric differential thermal analyses. New results on the thermal decomposition of bismuth oxalates under inert or reducing atmospheres are provided. On heating in nitrogen, both studied compounds decompose into small bismuth particles. Thermal properties of the metallic products were investigated. The Bi(C<sub>2</sub>O<sub>4</sub>)OH decomposition leads to a Bi–Bi<sub>2</sub>O<sub>3</sub> metal–oxide composite product in which bismuth is confined in a nanometric size, due to surface oxidation. The melting point of such bismuth particles is strongly related to their crystallite size. The nanometric bismuth melting has thus been evidenced ~40 °C lower than for bulk bismuth. These results should contribute to the development of the oxalate precursor route for low-temperature soldering applications.



## INTRODUCTION

The properties of nanoparticles and nanomaterials have been attracting the attention of physicists, chemists, and engineers since long ago. The increase of surface-to-volume ratio as the particle size shrinks enhances the surface properties.<sup>1</sup> The melting-point depression phenomenon is known to be resulting from the higher surface energy of small nanoparticles. This effect was predicted a long time ago by Pawlow<sup>2</sup> and first studied by Takagi<sup>3</sup> on various metal thin films (Pb, Sn, and Bi). Although low melting can be an issue for some applications of nanomaterials, this property is promising to offer answers to electronic packaging challenges. It is identified as a way to lower the joining process temperatures.<sup>1,4</sup> On the basis of this concept, a new kind of assembly method for power electronics was formerly developed with silver oxalate as a precursor for high thermal conductivity sintered silver interfaces.<sup>5,6</sup> The thermal decomposition of the silver oxalate into metal nanoparticles with a high propensity for sintering allows a low-temperature joining process. With the will to broaden the oxalate precursor route for low-temperature soldering, several compounds other than silver oxalate were studied. Relying on the various alloying elements that are considered in the development of lead-free soldering technology (Ag, Cu, Bi, Sn,

In, Sb, Zn, ...),<sup>7</sup> the controlled thermal decomposition of bismuth oxalates into metallic bismuth particles was investigated in the present work. Bismuth is a low melting-point metal ( $T_m = 271.4$  °C<sup>8</sup>) the use of which in electronic packaging has been accentuated by needs for Restriction of Hazardous Substances (RoHS, European Union directive) compliance. Because of these health and environmental concerns, the low toxicity of bismuth makes it attractive and seriously considered as a replacement for lead in electronic devices.<sup>9,10</sup> Pure bismuth is known for its brittleness, high electrical resistivity, and low thermal conductivity.<sup>10</sup> It is also known for lowering the melting point of the metals it is alloyed with, so bismuth is mostly used as an alloying element in soldering applications. Low-melting (138 °C) tin–bismuth eutectic is appreciated for low-temperature assemblies. Bi-based alloys are also candidates for lead-free high-temperature applications: BiAg,<sup>11</sup> BiSbCu,<sup>10</sup> and BiCuSn.<sup>12</sup>

Numerous studies focused on the synthesis and the thermal decomposition of bismuth oxalates in the last decades. The thermolysis in air of Bi-containing mixed oxalates proved to be

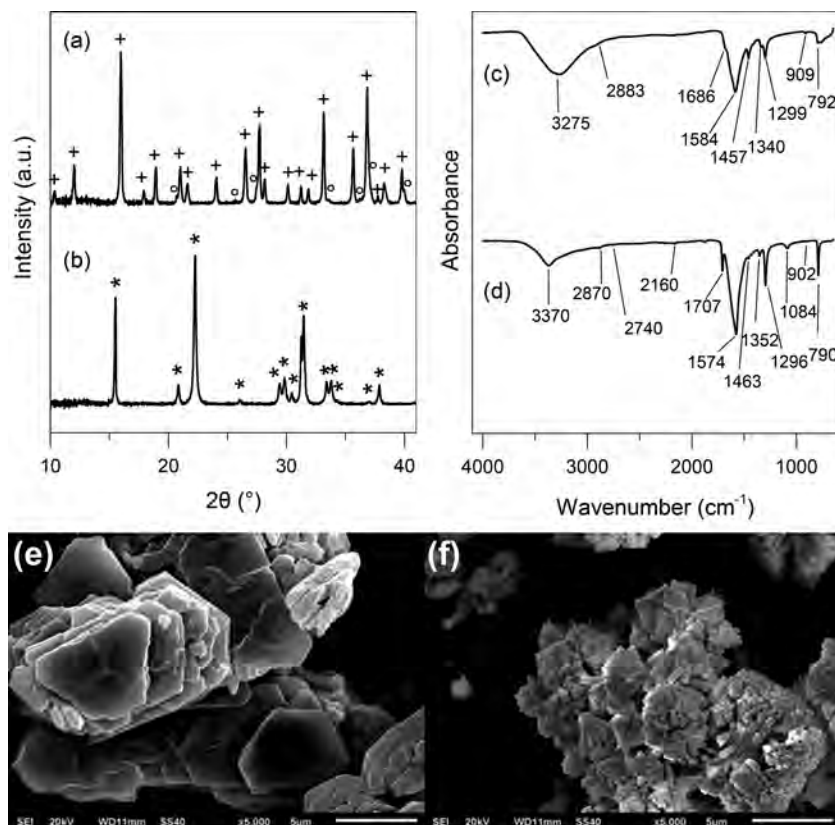


**Figure 1.** XRD patterns, IR spectra, and SEM images of OxBi(1) (a, c, e) and OxBi(2) (b, d, f). Bismuth oxalate XRD patterns were indexed:  $\text{Bi}_2(\text{C}_2\text{O}_4)_3 \cdot 7\text{H}_2\text{O}$ : (+) ref 26 and (°) lines indexed by calculation;  $\text{Bi}(\text{C}_2\text{O}_4)\text{OH}$ : (\*) refs 26 and 31.

a promising chemical route for the preparation of high- $T_c$  superconducting oxides<sup>13–15</sup> and ferroelectric materials.<sup>16,17</sup> Bismuth carboxylates have been used as precursors for the formation of bismuth–molybdate catalysts.<sup>18,19</sup> Various bismuth oxalate precursors were also studied for the synthesis of bismuth oxide with controlled morphology for photocatalytic<sup>20,21</sup> and electrochemical applications.<sup>22</sup> Several bismuth oxalate crystal structures have been described. The first ones reported were the compounds  $\text{Bi}_2(\text{C}_2\text{O}_4)_3 \cdot 7\text{H}_2\text{O}$  and  $\text{Bi}_2(\text{C}_2\text{O}_4)_3 \cdot \text{H}_2\text{C}_2\text{O}_4$ <sup>23</sup> (JCPDS 38–0548 and 38–0549). Others refinements were more recently performed, and the formulas were revised to lead, respectively, to  $\text{Bi}_2(\text{C}_2\text{O}_4)_3 \cdot 8\text{H}_2\text{O}$ <sup>24</sup> and  $\text{Bi}_2(\text{C}_2\text{O}_4)_3 \cdot 6\text{H}_2\text{O}$ <sup>24,25</sup> (ICSD 281570 and 281571). Tortet et al.<sup>26</sup> described the synthesis, the crystal structure refinement from XRD powder data, and the thermal behavior in air of three different bismuth oxalates:  $\text{Bi}_2(\text{C}_2\text{O}_4)_3 \cdot 7\text{H}_2\text{O}$ ,  $\text{Bi}_2(\text{C}_2\text{O}_4)_3 \cdot 6\text{H}_2\text{O}$ , and  $\text{Bi}(\text{C}_2\text{O}_4)\text{OH}$ . The third one is the object of very recent studies,<sup>27–30</sup> as bismuth-containing compounds are considered as a novel type of photocatalytic materials.<sup>31,32</sup> Its crystal structure was described by Rivenet et al.<sup>33</sup> from single-crystal data (ICSD 419313).

Although the interest of metal–organic decomposition route to produce metals has already been stated,<sup>34–37</sup> the thermal behavior of bismuth oxalates, to our knowledge, was mainly studied in air to produce bismuth oxide. In older investigations on the thermal decomposition of various metal oxalates, Dollimore et al. reported results of thermal studies on a commercial sample of bismuth oxalate to which the formula  $\text{Bi}_2(\text{C}_2\text{O}_4)_3 \cdot 4\text{H}_2\text{O}$  was ascribed. The decomposition reaction was found to be endothermic,<sup>38</sup> and the decomposition product in nitrogen was a mixture of bismuth and bismuth oxide.<sup>39</sup>

Monnereau et al.<sup>40</sup> performed analyses under vacuum and decomposed  $\text{Bi}_2(\text{C}_2\text{O}_4)_3 \cdot 7\text{H}_2\text{O}$  and  $\text{Bi}_2(\text{C}_2\text{O}_4)_3 \cdot 6\text{H}_2\text{O}$  into bismuth and a third compound  $\text{Bi}(\text{C}_2\text{O}_4)\text{OH}$  into a mixture of metal and oxide.

In this paper, the results of a study on two different bismuth oxalates, namely,  $\text{Bi}_2(\text{C}_2\text{O}_4)_3 \cdot 7\text{H}_2\text{O}$  and  $\text{Bi}(\text{C}_2\text{O}_4)\text{OH}$ , are presented. The oxalate powders were synthesized and characterized to understand the influence of the atmosphere on their thermal behavior and their decomposition products. The conditions of the production of bismuth particles and their thermal (melting and solidification) properties were investigated.

## ■ EXPERIMENTAL SECTION

Bismuth salt  $\text{Bi}(\text{NO}_3)_3 \cdot 5\text{H}_2\text{O}$  (Acros Organics, 98%) and oxalic acid  $\text{H}_2\text{C}_2\text{O}_4 \cdot 2\text{H}_2\text{O}$  (VWR, 99.5%) were used as starting materials for the synthesis of bismuth oxalates. According to the procedure described by Tortet et al.,<sup>26</sup> bismuth nitrate was dissolved in molar nitric acid, and oxalic acid was dissolved in water. The respective solution concentrations were 0.2 M and 0.3M. Both solutions were slowly added to a pH-controlled aqueous solution. The pH of the reaction mixture was adjusted before and during the precipitation, as appropriate, with hydrochloric acid or ammonia. The precipitation occurred under constant stirring (250 rpm). The white powders were filtrated after 1 h of aging and then washed with ethanol and dried under air at room temperature. Below pH < 1 and with 10% excess of oxalic acid solution, oxalate sample was called OxBi(1). With pH > 7 and 10% excess of bismuth nitrate solution, oxalate sample was called OxBi(2).

The oxalate powders and their thermal decomposition solid products were observed by scanning electron microscopy (SEM) using a JEOL JSM-6510 LV (SEM, 20 kV) and a JEOL JSM-7800F (field-emission guns–scanning electron microscopy (FEG-SEM), 5

kV). Phase detection was performed by X-ray diffraction using a Bruker D4 Endeavor diffractometer. Temperature-dependent X-ray diffraction (TDXRD) measurements were performed with a Bruker D8 diffractometer in air or nitrogen flow. The samples were heated in an Anton Paar HTK 1200N heating chamber with a heating rate of 2 °C/min. The temperature values were corrected in the TDXRD data after a calibration performed with the bulk melting measurement of tin ( $T_m = 232$  °C) and bismuth samples ( $T_m = 271$  °C). The diffractometers were both equipped with a one-dimensional (1D) LynxEye detector ( $\lambda_{\text{CuK}\alpha 1,2}$ , scan step increment = 0.02°, counting time = 0.13 s/step). Bismuth particle sizes were estimated by using the Scherrer equation.<sup>41,42</sup> The Bi (104) diffraction line broadening was measured with full width at half-maximum (fwhm), and the instrumental broadening was determined with standard Al<sub>2</sub>O<sub>3</sub> sintered discs (corundum, NIST SRM 1976). For the Scherrer constant, the typical value of 0.9 was used. The oxalates infrared spectra were recorded (4000–600 cm<sup>-1</sup>) using a Nexus Thermo Nicolet spectrometer. Thermogravimetric differential thermal analyses coupled with infrared spectrometry (TG-DTA-IR) were performed in several atmospheres (air, nitrogen, hydrogen) with a heating rate of 2 °C/min on a Setaram Setsys Evolution analyzer. The gases produced by oxalate decomposition were collected at the thermobalance outflow, and then the CO<sub>2</sub> infrared signal was measured using a Thermo Scientific Nicolet iS10 spectrometer.

## RESULTS AND DISCUSSION

**Bismuth Oxalates Structural and Morphological Characteristics.** XRD powder analysis allowed to confirm the crystal structures and formulas of OxBi(1) and OxBi(2) samples. Both bismuth oxalate XRD patterns were identified (Figure 1a,b), according to previous work.<sup>26,33</sup> Concerning OxBi(1), phase identification was made thanks to results obtained by Tortet et al.<sup>26</sup> who refined the lattice constants of a hexagonal cell ( $a = 9.932$  Å and  $c = 14.635$  Å) for the heptahydrated bismuth oxalate Bi<sub>2</sub>(C<sub>2</sub>O<sub>4</sub>)<sub>3</sub>·7H<sub>2</sub>O. Additional lines ( $2\theta = 20.6^\circ, 25.6^\circ, 27.4^\circ, 33.5^\circ, 36.1^\circ, 37.2^\circ,$  and  $39.9^\circ$ ), not reported by Tortet et al.,<sup>26</sup> were also assigned to the Bi<sub>2</sub>(C<sub>2</sub>O<sub>4</sub>)<sub>3</sub>·7H<sub>2</sub>O compound, based on the reported lattice parameters. For OxBi(2), results are consistent with data from Rivenet et al.<sup>33</sup> who solved the bismuth oxalate hydroxide Bi(C<sub>2</sub>O<sub>4</sub>)OH structure from single crystals (orthorhombic cell, space group *Pnma*,  $a = 6.0853$  Å,  $b = 11.4479$  Å, and  $c = 5.9722$  Å, ICSD 419313) and also from Tortet et al.<sup>26</sup> who refined cell parameters from powder XRD measurements (orthorhombic cell,  $a = 11.427$  Å,  $b = 6.072$  Å, and  $c = 5.971$  Å). So we were able to assign the formulas Bi<sub>2</sub>(C<sub>2</sub>O<sub>4</sub>)<sub>3</sub>·7H<sub>2</sub>O and Bi(C<sub>2</sub>O<sub>4</sub>)OH, respectively, to our samples OxBi(1) and OxBi(2).

IR spectra of OxBi(1) and OxBi(2) are similar (Figure 1c,d). The results are in agreement with works reported in the literature.<sup>25,26,43</sup> They are given in Table 1. The bands between 3700 and 2500 cm<sup>-1</sup> are ascribed to  $\nu_{\text{O-H}}$  stretching modes. Between 1710 and 700 cm<sup>-1</sup>, we find the characteristic signals of the oxalate anion C<sub>2</sub>O<sub>4</sub><sup>2-</sup> and Bi–O bond vibrations. For OxBi(2), Tortet et al.<sup>26</sup> assigned some bands, which are not present in OxBi(1) spectrum, to vibration modes related to Bi–O–H entities in the Bi(C<sub>2</sub>O<sub>4</sub>)OH compound:  $\nu_{\text{Bi-O-H}}$  stretching modes (2740 and 2160 cm<sup>-1</sup>) and a  $\delta_{\text{Bi-O-H}}$  in-plane bending mode (1084 cm<sup>-1</sup>). The hydroxyl group was thereafter described by Rivenet et al.<sup>33</sup> in the Bi(C<sub>2</sub>O<sub>4</sub>)OH structure.

The morphology determination by SEM imaging allowed to verify the product homogeneity and the accordance with previous observations reported in the literature.<sup>21,22,26–29</sup> The particles from OxBi(1) sample are aggregates of nearly hexagonal flakes with 5–10 μm dimensions (Figure 1e). The

**Table 1.** IR Data for OxBi(1) and OxBi(2)<sup>26</sup>

IR vibration mode	wavenumber (cm <sup>-1</sup> )	
	OxBi(1)	OxBi(2)
$\nu_{\text{O-H}}$ stretching	3275	3370
combination	1584 + 1299 = 2883	1574 + 1296 = 2870
$\nu_{\text{Bi-O-H}}$ stretching		2740 2160
$\nu_{\text{C=O}}$ stretching	1686 (shoulder) 1584	1707 1574
$\nu_{\text{C-O}}$ and $\nu_{\text{C-C}}$ stretching	1457 1340	1463 1352
$\nu_{\text{C-O}}$ stretching and $\delta_{\text{O-C=O}}$ bending	1299	1296
$\delta_{\text{Bi-O-H}}$ in plane bending		1084
$\nu_{\text{C-O}}$ stretching and $\delta_{\text{O-C=O}}$ bending	909	902
$\delta_{\text{O-C=O}}$ bending and $\nu_{\text{Bi-O}}$ stretching	792	790

OxBi(2) powder is made of bundles of 2–3 μm long needle-shaped particles (Figure 1f).

**Thermal Study.** The understanding of the thermal behavior of the different bismuth oxalates was based on results from several techniques: thermogravimetry coupled with differential thermal analysis (in air, N<sub>2</sub> and H<sub>2</sub> atmospheres), TDXRD (in air and N<sub>2</sub>), SEM, and FEG-SEM imaging of intermediate and final products obtained under oxygen-free atmospheres. Thermal decomposition of Bi<sub>2</sub>(C<sub>2</sub>O<sub>4</sub>)<sub>3</sub>·7H<sub>2</sub>O and Bi(C<sub>2</sub>O<sub>4</sub>)OH under nitrogen and hydrogen has not been reported yet in literature.

**Thermal Behavior of OxBi(1). In Air.** On the thermogram recorded in air (Figure 2a), oxalate dehydration, which is endothermic, occurs in two steps between 30 and 220 °C. The first one corresponds to the departure of five water molecules, and the second one corresponds to the departure of the remaining two water molecules, as Tortet et al. explained.<sup>26</sup> Above 220 °C, a more important weight loss, associated with two exothermic peaks, corresponds to the decomposition of anhydrous bismuth oxalate Bi<sub>2</sub>(C<sub>2</sub>O<sub>4</sub>)<sub>3</sub> into bismuth oxide Bi<sub>2</sub>O<sub>3</sub>. Global weight variation of 42.2% is close to the theoretical value (42.33%). Temperature-dependent XRD measurements allowed us to follow the thermal decomposition stages of the bismuth oxalate (Figure 2c). OxBi(1) X-ray diffraction pattern changes from room temperature to 200 °C, which means that dehydration has an influence on compound crystal structure. Anhydrous bismuth oxalate obtained at 200 °C does not display well-defined diffraction peaks. It can then be assumed to be very badly crystallized. This observation was also reported by Tortet et al.<sup>26</sup> Tetragonal β-Bi<sub>2</sub>O<sub>3</sub> XRD pattern (JCPDS 27–0050) is visible at 250 °C, which confirms older results<sup>40</sup> about the decomposition of anhydrous bismuth oxalate into the metastable bismuth oxide form, usually observed at high temperature by cooling the cubic δ-Bi<sub>2</sub>O<sub>3</sub> phase.<sup>44,45</sup> Then, another transition is observed between 350 and 400 °C, from β-Bi<sub>2</sub>O<sub>3</sub> to the stable monoclinic α-Bi<sub>2</sub>O<sub>3</sub> form (JCPDS 70–8243), which was previously reported.<sup>33,40</sup> Depending on the final temperature of the heat treatment (Figure S1), we were able to stabilize the β form at room temperature. A final phenomenon, which is not displayed on Figure 2c, occurs between 700 and 740 °C. It is the transition from the monoclinic α-Bi<sub>2</sub>O<sub>3</sub> phase to the high-temperature cubic δ-Bi<sub>2</sub>O<sub>3</sub> phase (JCPDS 74–1633), also revealed by a

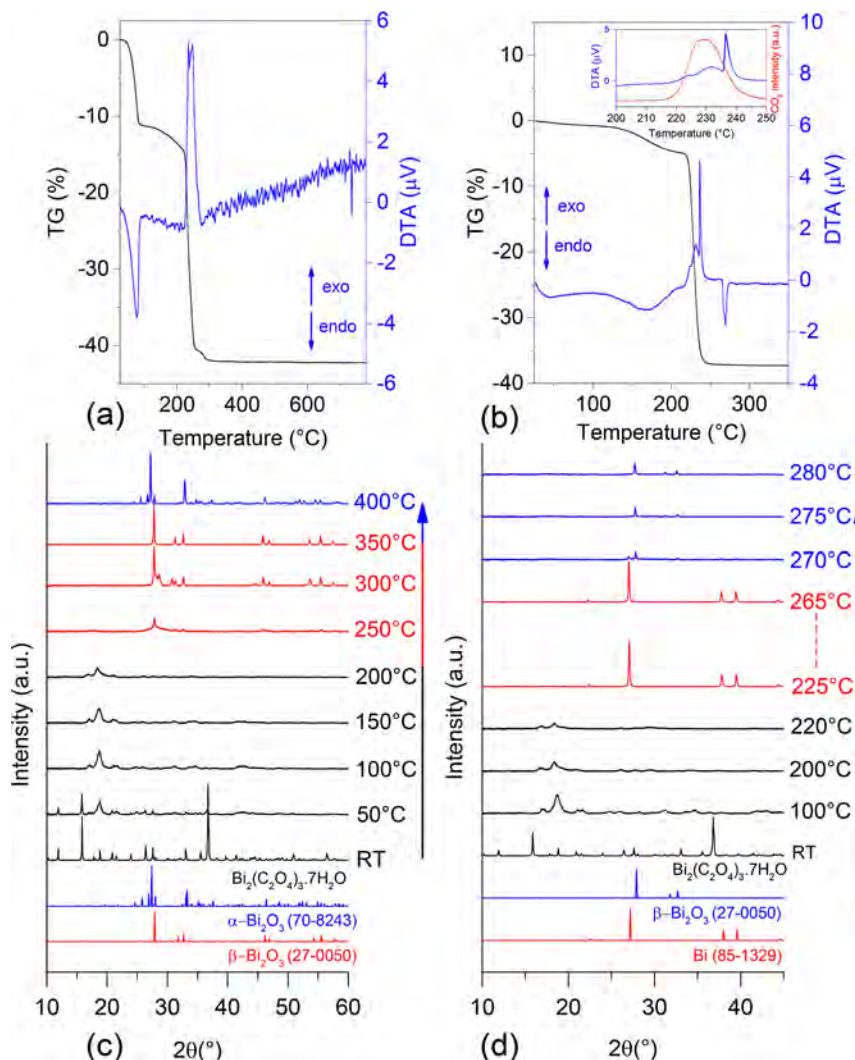


**Figure 2.** TG-DTA-IR data for OxBi(1) in air (a) and N<sub>2</sub> (b); TDXRD patterns for OxBi(1) in air (c) and N<sub>2</sub> (d).

small endothermic peak (736 °C) in the TGA/DTA experiment (Figure 2). The study of the cooling part (Figure S2 and Figure S3a) highlighted two well-known phase transitions of Bi<sub>2</sub>O<sub>3</sub>:<sup>44,45</sup> a  $\delta$ -Bi<sub>2</sub>O<sub>3</sub> to  $\beta$ -Bi<sub>2</sub>O<sub>3</sub> transition (revealed by HTXRD at  $\sim$ 650 °C and an DTA exothermic peak at 658 °C) and a  $\beta$ -Bi<sub>2</sub>O<sub>3</sub> to  $\alpha$ -Bi<sub>2</sub>O<sub>3</sub> transition (revealed by HTXRD at  $\sim$ 550 °C and by DTA at 531 °C).

*In Nitrogen.* The thermal behavior of OxBi(1) under nitrogen can be understood as follows. A first weight loss (11.0%), which does not appear on the thermogram, occurs during the vacuum purge ( $\sim 1 \times 10^{-2}$  mbar) performed before filling the furnace with inert gas. It is assigned to the departure of five water molecules (theory: 11.1%). A second loss (5.0%) is recorded between 100 and 215 °C (Figure 2b), corresponding to the departure of the remaining two water molecules. Again, the dehydration phenomenon is endothermic. Between 215 and 250 °C, a more important weight loss of 32.4% is assigned to the exothermic decomposition of anhydrous bismuth oxalate Bi<sub>2</sub>(C<sub>2</sub>O<sub>4</sub>)<sub>3</sub> into metallic bismuth. The exothermic nature of the decomposition is not in agreement with the DTA results reported by Dollimore et al.<sup>38</sup> from a commercial bismuth oxalate with the formula Bi<sub>2</sub>(C<sub>2</sub>O<sub>4</sub>)<sub>3</sub>·4H<sub>2</sub>O. The sharp exothermic peak observed at 236 °C in Figure 2c does not seem to be related to the CO

oxidation into CO<sub>2</sub>, already mentioned in the literature,<sup>26,46</sup> but rather a crystallization process, due to the temperature-dependent growth of small bismuth particles formed at the beginning of the decomposition. Indeed, the CO<sub>2</sub> departure peak related to the bismuth oxalate decomposition is offset from the crystallization supposed peak (inset in Figure 2c). The global weight loss of 48.4% is quite close to the calculated value for the decomposition of heptahydrated bismuth oxalate into pure metallic bismuth (48.27%). So we can suggest the following equation for the global decomposition reaction in nitrogen:  $\text{Bi}_2(\text{C}_2\text{O}_4)_3 \cdot 7\text{H}_2\text{O} \rightarrow 2 \text{Bi} + 6 \text{CO}_2 + 7 \text{H}_2\text{O}$ . A further endothermic peak is ascribed to the melting of bismuth. The peak broadness (264–272 °C) suggests a few degrees melting range, but the values can be assimilated to a bismuth bulk behavior ( $T_m = 271.4$  °C<sup>8</sup>). The metallic nature of the decomposition product was confirmed by XRD. The diffraction pattern was in accordance with the JCPDS file 85–1329 (Figure 3a). It was also revealed that samples that were heated above the bismuth melting point were subjected to a partial oxidation (Figure 3b). Additional diffraction peaks were assigned to  $\beta$ -Bi<sub>2</sub>O<sub>3</sub>, although no significant weight gain was noted on the thermogram above the melting temperature. This may be understood as an increase of the bismuth sensitivity to surface oxidation due to the liquid state. It means that the inert

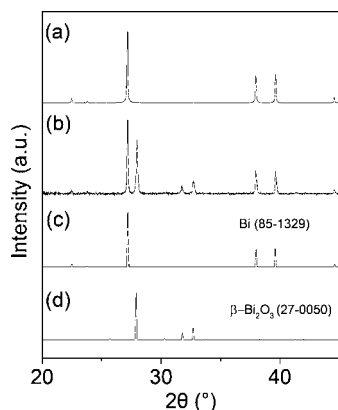


**Figure 3.** XRD patterns of OxBi(1) decomposition products in  $N_2$ : below the bismuth melting point (a) and above the bismuth melting point (b). Bi, JCPDS 85-1329 (c),  $\beta$ - $Bi_2O_3$ , JCPDS 27-0050 (d).

atmosphere is not totally free of oxygen. It was observed in temperature-dependent XRD measurements that, from room temperature to 200 °C, OxBi(1) X-ray diffraction pattern is the same in nitrogen as in air (Figure 2d). The same badly crystallized compound is obtained after dehydration. At 225 °C, the metallic bismuth diffraction peaks confirm that OxBi(1) decomposes into metal particles under an inert atmosphere. At  $\sim 270$  °C, the metal peak intensity strongly decreases, and small  $\beta$ - $Bi_2O_3$  peaks show the beginning of a temperature-dependent bismuth oxidation phenomenon. At 275 °C, the bismuth XRD pattern is not visible anymore, which confirms the metal melting measured by DTA (Figure 2d). Only the bismuth oxide diffraction peaks can be seen, getting more intense with temperature because of the increasing oxidation kinetics. SEM imaging allowed to follow the OxBi(1) morphological evolution during its thermal decomposition (Figure 4). OxBi(1) samples were heated in nitrogen at different temperatures then cooled before being observed. It was first found that the oxalate particle morphology is not modified by dehydration. The decomposition product obtained at 250 °C in  $N_2$  is made of a porous and microstructured bismuth network (Figure 4b). When the sample was heated above the bismuth melting point, the decomposition product was made of shiny metallic rounded particles with dimensions varying between 50 and 200  $\mu m$  (Figure 4c).

**In Hydrogen.** TG-DTA data obtained under pure hydrogen for OxBi(1) was quite similar to the one under nitrogen. The decomposition temperature and the total weight loss are the

same as those described above. Nevertheless, the reducing atmosphere allows to get a pure metallic product without traces of bismuth oxide, regardless of the maximum temperature treatment.

**Thermal Behavior of OxBi(2). In Air.** Regarding OxBi(2) thermogram in air (Figure 5), a first slight weight loss is recorded between 30 and 215 °C, before the decomposition into  $Bi_2O_3$  between 215 and 300 °C, associated with an exothermic peak. The global weight loss (25.8%) is equal to the theoretical value. For samples treated at 300 and 400 °C, the solid products were, respectively, the  $\beta$  (tetragonal, metastable) and  $\alpha$  (monoclinic, stable at room temperature) polymorphs of  $Bi_2O_3$ , as described before in the study of the thermal behavior of OxBi(1). Monnereau et al.<sup>40</sup> already noticed the possibility to stabilize the  $\beta$ - $Bi_2O_3$  phase (generally observed at high temperature), by decomposition of both bismuth oxalates described here. Rivenet et al.<sup>33</sup> assigned a small exothermic peak to the transition from  $\beta$ - $Bi_2O_3$  to  $\alpha$ - $Bi_2O_3$  during the TGA of  $Bi(C_2O_4)OH$  in air. This peak did not seem to be present in our work. Another endothermic peak was recorded at 736 °C (Figure 5). It is ascribed to the phase transition from  $\alpha$ - $Bi_2O_3$  to  $\delta$ - $Bi_2O_3$ . A TD-XRD study of  $Bi(C_2O_4)OH$  in air was already reported by Rivenet et al.<sup>33</sup> They proposed the following reaction:  $Bi(C_2O_4)OH \rightarrow \beta$ - $Bi_2O_3 \rightarrow \alpha$ - $Bi_2O_3 \rightarrow \delta$ - $Bi_2O_3$ . It was confirmed in the present work (Figure 5c). The  $\alpha$ - $Bi_2O_3$  to  $\delta$ - $Bi_2O_3$  transition between 700 and 730 °C is not displayed on the figure. The study of the cooling part highlighted the same two phase transitions as for OxBi(1):  $\delta$ - $Bi_2O_3$  to  $\beta$ - $Bi_2O_3$  (between 700 and 600 °C) and  $\beta$ - $Bi_2O_3$  to  $\alpha$ - $Bi_2O_3$  (between 600 and 500 °C), already demonstrated by DTA (Figure S3b).

**In Nitrogen.** Concerning the OxBi(2) thermogram in nitrogen, a first very slight weight loss is observed between 30 and 230 °C, before the endothermic bismuth oxalate decomposition between 230 and 320 °C. The global mass variation (29.3%) is lower than the theoretical value (33.44%) for the decomposition of bismuth oxalate hydroxide into metallic bismuth. The reason for this difference was determined by XRD. Indeed, the metallic product of thermal decomposition proved to be partially oxidized, even at temperatures below the bulk bismuth melting point (271 °C). It can be noticed that no endothermic phenomenon is observed at  $\sim 271$  °C, where we could expect the melting of bismuth. This could be explained by a lowered melting point of the metallic product due to the very small size of first bismuth particles. Knowing that the metal oxalate decomposition begins with the formation of metallic nanoparticles,<sup>5,36</sup> we could explain this early liquid

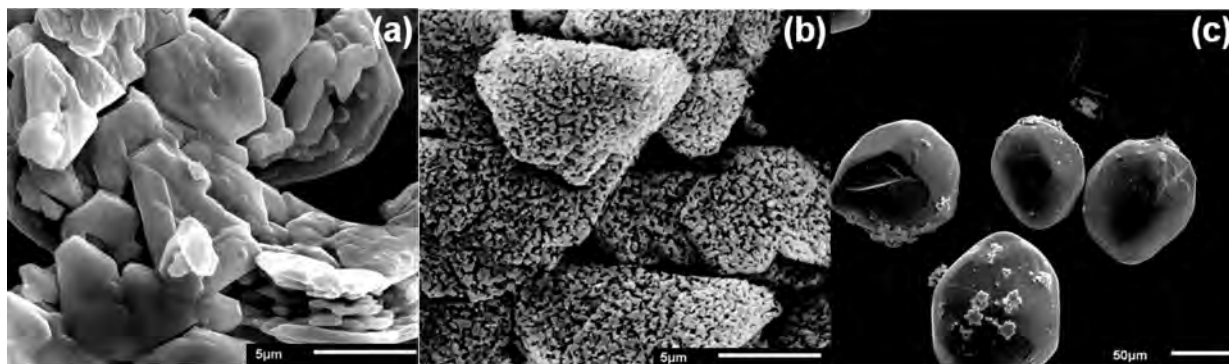


**Figure 4.** OxBi(1) thermal decomposition steps in  $N_2$ : before decomposition (a); after decomposition into bismuth at 250 °C (b); after bismuth melting at 300 °C (c).

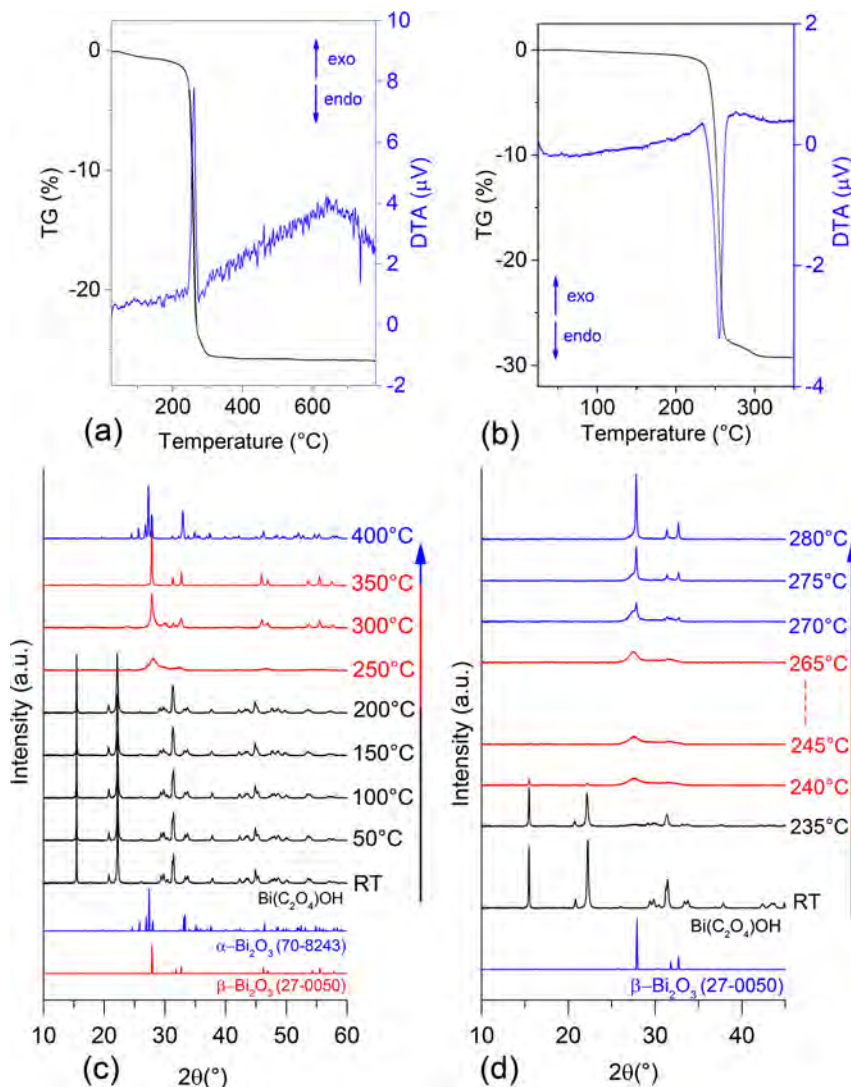


**Figure 5.** TG-DTA data for OxBi(2) in air (a) and N<sub>2</sub> (b); TDXRD pattern for OxBi(2) in air (c) and N<sub>2</sub> (d).

state of bismuth by the size dependency of the melting temperature.<sup>47</sup> The presence of bismuth oxide in the decomposition product without heating above 271 °C also confirms this noteworthy behavior, because it was previously noticed that molten bismuth is more likely to oxidize. The final mixture of Bi and  $\beta$ -Bi<sub>2</sub>O<sub>3</sub> was also obtained by Monnereau et al.<sup>40</sup> with the same bismuth oxalate in vacuum. We can likewise bring these results closer to those obtained by Dollimore et al.<sup>38,39</sup> with a commercial bismuth oxalate. Indeed, they reported an endothermic decomposition without any bismuth melting peak as well as a mixture of bismuth and bismuth oxide as the decomposition product. These results being similar to ours, we could presume that the commercial sample they decomposed at the time was of type Bi(C<sub>2</sub>O<sub>4</sub>)OH and not Bi<sub>2</sub>(C<sub>2</sub>O<sub>4</sub>)<sub>3</sub>·4H<sub>2</sub>O as ascribed by the authors. So we can suggest the following equation for the global decomposition reaction in nitrogen:  $6 \text{ Bi}(\text{C}_2\text{O}_4)\text{OH} \rightarrow 4 \text{ Bi} + \text{Bi}_2\text{O}_3 + 12 \text{ CO}_2 + 3 \text{ H}_2\text{O}$ . TDXRD data in N<sub>2</sub> (Figure 5d) allowed to clarify the TG-DTA results for OxBi(2). At 240 °C, the Bi(C<sub>2</sub>O<sub>4</sub>)OH XRD pattern has almost disappeared, and it is possible to discern two bumps between 26° and 33°, where we could expect bismuth and bismuth oxide peaks: Bi(100),  $\beta$ -Bi<sub>2</sub>O<sub>3</sub> (201),  $\beta$ -Bi<sub>2</sub>O<sub>3</sub> (002), and  $\beta$ -Bi<sub>2</sub>O<sub>3</sub> (220). The bumps start being replaced by three

better-defined  $\beta$ -Bi<sub>2</sub>O<sub>3</sub> peaks from 270 °C, and these peaks get more intense with increasing temperature. It is important to note that no metallic Bi diffraction peak is visible during the heating part. However, first signals related to rhombohedral metallic bismuth appear at 190 °C by cooling the sample (Figure S6). This temperature can be assigned to the bismuth solidification point, which is consistent with the exothermic phenomenon measured at 185 °C by DTA (Figure S4b). These results mean that the OxBi(2) decomposition mechanism in an inert atmosphere implies the reaction from solid bismuth oxalate to liquid metallic bismuth. The nanosized bismuth product partially oxidizes as soon as it is formed, due to its enhanced surface reactivity and the residual oxygen partial pressure. Although no bismuth melting signal can be measured during the heating, the study of the cooling part allowed to highlight the crystallization phenomenon and confirm that bismuth was melted before. To corroborate these assumptions about an early melting behavior due to particle size dependency, an additional TDXRD experiment was performed (Figure 6) with a maximal temperature of 250 °C (21 °C below the bismuth bulk melting point). The same behavior was observed: no Bi diffraction peak was visible until the product of decomposition was cooled. The metal diffraction pattern

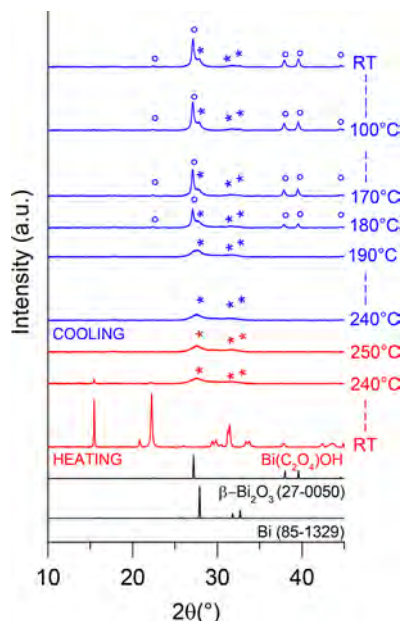


**Figure 6.** TDXRD pattern for OxBi(2) in nitrogen with maximum temperature of 250 °C. Decomposition products patterns were indexed: (deg) Bi, JCPDS 85–1329 ; (\*)  $\beta$ -Bi<sub>2</sub>O<sub>3</sub>, JCPDS 27–0050.

appears at 180 °C. The  $\beta$ -Bi<sub>2</sub>O<sub>3</sub> diffraction pattern is slightly visible but much less defined than for the experiment with a higher maximum temperature (Figure 5d and Figure S6), because the bismuth oxidation depends on temperature and time. Although the metal is molten during the OxBi(2) thermal analyses, the final decomposition product is a powder. Because of the partial oxidation of the freshly formed bismuth nanoparticles, the molten metallic material does not form a single drop but can be understood as a set of nanodroplets, each one being covered by a solid oxide shell that prevents the metal from coalescence at low temperature. A similar behavior has been reported with bismuth nanowires<sup>48</sup> that were annealed at 300 °C and maintained their morphology due to a thin protective oxide layer encasing the molten metal. In a bismuth–ceramic nanocomposite, Meitl et al.<sup>49</sup> also noticed the persistence of the bismuth nanostructure after melting and freezing. Another TG-DTA experiment with several successive heating cycles was performed to support this idea. The results will be discussed at the end of this work.

To explain the thermal properties differences among the metallic products obtained from OxBi(1) and OxBi(2) decomposition, it is possible to compare the thermal behavior of the two bismuth oxalates (Figure 7). On the one hand, the thermal events related to OxBi(1) decomposition and bismuth melting are clearly distinct. On the other hand, the OxBi(2) decomposition in nitrogen is not even complete at the bulk bismuth melting point, because there is a small weight loss (~2%) from 265 to 320 °C in addition to the main variation (Figure 5b). The TG-DTA experiments revealed there is a temperature shift between the decomposition processes of the two studied compounds (~20 °C at the beginning and 70 °C at the end). The endothermic character and the higher temperature for the OxBi(2) decomposition must be related to the hydroxyl group, which is present in the Bi(C<sub>2</sub>O<sub>4</sub>)OH structure,<sup>33</sup> contrary to the OxBi(1) compound. Indeed, it was found that the bismuth hydroxide Bi(OH)<sub>3</sub> decomposition is endothermic and begins at 390 °C.<sup>50</sup> No bismuth melting

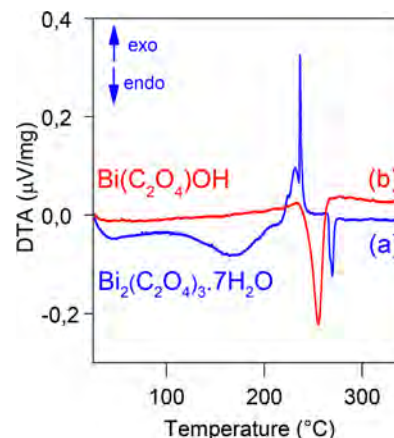


**Figure 7.** DTA comparison between OxBi(1) (a) and OxBi(2) (b) in N<sub>2</sub>.

peak can be seen in TG-DTA data for OxBi(2) at ~271 °C, because bismuth nanoparticles produced from the OxBi(2) decomposition are already melted but also separated from each other by protective bismuth oxide shells that prevent them from coalescing. The thermal closeness between OxBi(2) decomposition and bismuth melting must be responsible for the thermal events overlapping; thus, the Bi(C<sub>2</sub>O<sub>4</sub>)OH decomposition into liquid bismuth is accompanied by a single intense endothermic peak (Figure 7).

*In Hydrogen.* During the TG-DTA experiment with OxBi(2) in pure hydrogen, a larger weight loss (32.8%) was measured compared to the one in nitrogen (29.3%). The final decomposition product consisted of quite big shiny metallic balls (200–300 μm diameter), and the XRD analysis confirmed it was pure bismuth contrary to the study in nitrogen. The comparison of the OxBi(2) decomposition products under nitrogen and hydrogen made it possible to demonstrate the consequences of the surface oxidation on the bismuth particle ability to coalesce.

*Melting/Solidification Measurements in N<sub>2</sub>.* To measure the bismuth nanoparticle melting and solidification points, we tried to rely on the fact that the surface oxidation maintains the nanoparticles isolated from each other. If the temperature is not raised too much above the bismuth melting point, this oxide shell allows the nanoparticles to keep the thermal properties related to their size when cooled. In a single TG-DTA experiment in N<sub>2</sub>, an OxBi(2) sample was heated and cooled eight times. The maximum programmed temperature was increased by 10 °C at each cycle and varied from 240 to 310 °C to study the heat treatment temperature-dependency of the particle size (Figure 8 and Table 2). It was possible to measure a first solidification temperature in cycle No. 3 ( $T_s = 168.0$  °C) and a first melting temperature in cycle No. 4 ( $T_m = 254.0$  °C). The first measurable exothermic crystallization peak suggests that bismuth melting already occurred during the heating part of cycle No. 3. The associated DTA event could be the slight signal that is noticeable at ~251 °C (Figure 8a). First, it can be seen that the measured melting temperatures are lower than the bulk bismuth value. It is also important to note that the melting and solidification temperatures increase after each heating/cooling cycle. On the basis of the size-dependent melting model for nanoparticles,<sup>47,51</sup> it means that the OxBi(2) metallic decomposition product is nanosized and also that the particle size increases progressively due to successive heating. Limmer

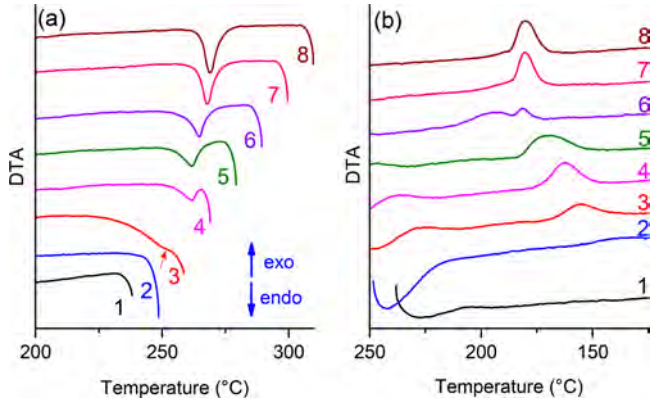


**Figure 8.** OxBi(2) DTA data for thermal cycling in nitrogen: heating (a) and cooling (b). (1)  $T_{\max} = 240$  °C; (2)  $T_{\max} = 250$  °C; (3)  $T_{\max} = 260$  °C; (4)  $T_{\max} = 270$  °C; (5)  $T_{\max} = 280$  °C; (6)  $T_{\max} = 290$  °C; (7)  $T_{\max} = 300$  °C; (8)  $T_{\max} = 310$  °C.

**Table 2.** OxBi(2) TG-DTA Data for Thermal Cycling<sup>a</sup> in Nitrogen

cycles	$T_{\max}$ (°C)	weight loss (%)	$T_m$ (°C)	$T_s$ (°C)
1	240	2.22		
2	250	11.62		
3	260	15.18	251 <sup>b</sup>	168.0
4	270	0.71	254.0	174.8
5	280	0.59	255.0	182.9
6	290	0.69	258.0	(212.6) 187.9
7	300	0.35	263.1	186.9
8	310	0.16	266.3	187.0

<sup>a</sup> $T_{\max}$ : maximum temperature of the cycle.  $T_m$ : bismuth extrapolated onset melting-point temperature.  $T_s$ : bismuth extrapolated onset solidification temperature. <sup>b</sup>Estimated temperature.

et al.<sup>48</sup> similarly reported that the annealing of bismuth nanowires leads to both grain growth and morphology retention, because the bismuth oxide shell prevents the molten metal from coalescence if the sample is not heated too much above the melting point. Starting from the measurement of melting points, we were able to estimate the mean bismuth particle size in the decomposed OxBi(2) sample at different stages of the experiment. The melting-point depression phenomenon has already been studied for small bismuth particles.<sup>3,47,51–54</sup> Most models that are used to describe the size dependency of nanoparticle melting point have the following form:<sup>47</sup>

$$T_m(r) = T_m^{\text{bulk}} - \left( \frac{2T_m^{\text{bulk}}}{H_m^{\text{bulk}} \rho_s} \right) \left( \frac{\alpha}{r} \right) = T_m^{\text{bulk}} - \left( \frac{A}{r} \right) \quad (1)$$

where  $T_m(r)$  is the size-dependent bismuth melting temperature,  $T_m^{\text{bulk}}$  is the bulk bismuth melting temperature,  $H_m^{\text{bulk}}$  is the bulk latent heat of fusion,  $\rho_s$  is the density of the solid phase, and  $\alpha$  is a parameter depending on the melting model. The homogeneous melting model (HMM) can be applied for bismuth nanoparticles.<sup>47,55</sup> It supposes a complete melting when  $T_m$  is reached, without any surface premelting process. So the parameter  $\alpha_{\text{HMM}}$  is expressed as follows:

$$\alpha_{\text{HMM}} = \sigma_{\text{SV}} - \sigma_{\text{LV}} \left( \frac{\rho_s}{\rho_L} \right)^{2/3} \quad (2)$$

where  $\sigma_{\text{SV}}$  is the energy of the solid–vapor interface,  $\sigma_{\text{LV}}$  is the energy of the liquid–vapor interface, and  $\rho_L$  is the density of the liquid phase. The data listed in Table 3 were used to

**Table 3.** Bismuth Data for Melting-Point Depression Model<sup>47,53</sup>

$T_m^{\text{bulk}}$	$H_m^{\text{bulk}}$	$\sigma_{\text{SV}}$	$\sigma_{\text{LV}}$	$\rho_s$	$\rho_L$
271.4 °C	51.9 J/g	550 mJ/m <sup>2</sup>	375 mJ/m <sup>2</sup>	9.8 g/cm <sup>3</sup>	10.1 g/cm <sup>3</sup>

calculate the values of  $\alpha_{\text{HMM}}$  and A:  $\alpha_{\text{HMM}} = 182$  mJ/m<sup>2</sup> and A = 390 nm·K. The use of the model and the experimental values of the melting temperature allowed to estimate the particle size value and its evolution with heat cycling in the last TG-DTA experiment (Figure 9): the mean bismuth nanoparticle size

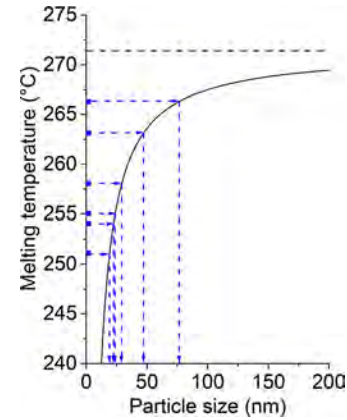


**Figure 9.** Estimation of bismuth nanoparticle size from the melting-point depression model and experimental melting-temperature measurements. Solid line: calculated from Equation 1; black dashed line: bulk melting point.

would vary between 19 and 77 nm. The crystallite size evolution as a function of treatment temperature was confirmed by applying the Scherrer equation to the peak broadening of bismuth (104) line ( $2\theta = 38.0^\circ$ ). This peak does not overlap with any other bismuth or bismuth oxide peak. OxBi(2) samples treated at 250 °C (Figure 6), 280 °C (Figure 5d), and 310 °C (Figure 8, cycle No. 8) resulted in different peak widths that allow to estimate crystallite sizes of 30, 45, and 90 nm, respectively. This result confirms that the bismuth nanocrystallite size increases with treatment temperature without reaching the bulk scale. The values are quite consistent with those calculated by the size-dependent melting model, knowing that it is the particle radius that is considered in the Equation 1. As a comparison between the metallic products obtained from the two different bismuth oxalates, the Scherrer equation allowed to estimate the crystallite size at 75 nm for OxBi(1) samples treated at 250 °C (Figure 4b), while no peak broadening is noted for samples treated above bulk bismuth melting point (Figure 4c). Although the bismuth melting-point depression is known to be mainly due to particle size,<sup>49,53,54</sup> Equation 1 was used in this work as a first approximation for size prediction. The interaction between the metal and the substrate is neglected in the HMM model. The Bi/Bi<sub>2</sub>O<sub>3</sub> interface, which explains the confinement of bismuth nanoparticles in this work, is not considered in the equation. Several studies on the melting of nanostructured bismuth embedded in various materials (metal,<sup>54</sup> metallic glass,<sup>56</sup> ceramic,<sup>49</sup> poly-

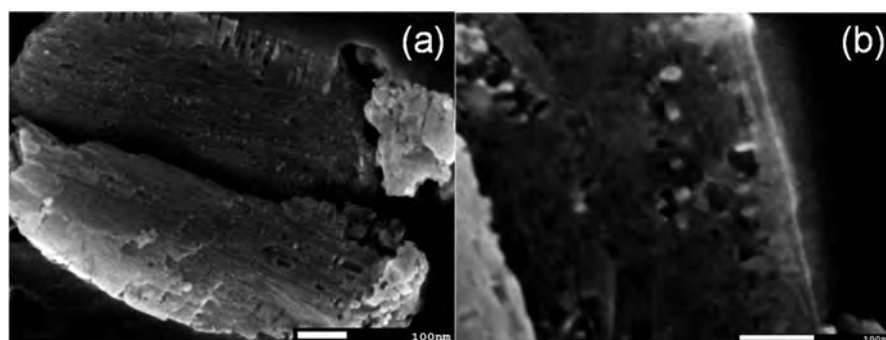


**Figure 10.** FEG-SEM observation: morphology of a partially decomposed  $\text{Bi}(\text{C}_2\text{O}_4)\text{OH}$  particle (treatment temperature:  $240\text{ }^\circ\text{C}$ ) (a) Bi nanoparticles on the oxalate precursor surface (b).

mer<sup>57</sup>) have been reported. The matrices allow to prevent nanoparticle coalescence and to repeat melting measurements. The hypothetical influence of the interface between the low-melting bismuth and the surrounding material was not clearly evidenced, and the melting behavior deviated from bulk was ascribed to size-dependency. However, size-dependent melting models that include the matrix factor have already been proposed for nanocrystals.<sup>58</sup> In our case, more work is needed to clarify the  $\text{Bi}/\text{Bi}_2\text{O}_3$  interface factor. An  $\text{OxBi}(2)$  sample was partially decomposed by stopping the thermal treatment at a maximum temperature of  $240\text{ }^\circ\text{C}$ . SEM-FEG observations allowed to reveal bismuth nanoparticles from the beginning of the oxalate precursor decomposition (Figure 10). On Figure 10a, the needlelike morphology of the oxalate can be recognized, and small bright bismuth particles (a few nanometers in size) can be seen on the surface. Figure 10b shows more clearly some bigger metal particles (20 to 30 nm).

## CONCLUSIONS

Two different bismuth oxalates were synthesized, and the atmosphere impact on their thermal decomposition products was investigated. The results obtained in air were in accordance with literature. New data are provided on the bismuth oxalate thermal behavior in inert atmospheres. The metallic decomposition products and their melting properties were studied. The most significant finding to emerge from this study is the low-temperature liquid state of the nanosized metallic product obtained from  $\text{Bi}(\text{C}_2\text{O}_4)\text{OH}$ . DTA measurements allowed to confirm the bismuth melting-point depression and to highlight that the metal is already melted when bismuth oxalate starts to decompose.  $\text{Bi}(\text{C}_2\text{O}_4)\text{OH}$  was partially decomposed to emphasize the nanoparticle production process. Multiple heat treatments in nitrogen revealed that nanoparticle size increased with heating temperature. However, the surface oxidation allowed the bismuth nanoparticles to stay confined and prevented them from very quick and complete coalescence above the metal melting point. The size-dependent melting model and the X-ray diffraction line broadening were used to estimate the bismuth particle size evolution. On the one hand, these results clearly show that the melting temperature of metallic bismuth, covered by a very thin oxide layer, is strongly dependent to the crystallite size when it is lower than 100 nm. On the other hand, the particle growth easily occurred in hydrogen, without any oxidation phenomenon, until the bulk bismuth melting properties were reached. The knowledge gained from this work on the lowering of the melting point of bismuth may be useful for the development of materials for low-temperature soldering.

## ASSOCIATED CONTENT

### Supporting Information

The Supporting Information is available free of charge on the ACS Publications website at DOI: [10.1021/acs.inorgchem.7b00608](https://doi.org/10.1021/acs.inorgchem.7b00608).

$\alpha$ -,  $\beta$ -, and  $\delta$ - $\text{Bi}_2\text{O}_3$  XRD patterns, DTA cooling data in air and nitrogen, TDXRD cooling data in nitrogen (PDF)

## AUTHOR INFORMATION

### Corresponding Author

\*E-mail: [pierre.roumanille@irt-saintexupery.com](mailto:pierre.roumanille@irt-saintexupery.com).

### ORCID

Pierre Roumanille: 0000-0003-2415-8251

### Notes

The authors declare no competing financial interest.

## ACKNOWLEDGMENTS

We thank Continental Automotive, Inventec Performance Chemicals, and Thales Alenia Space for funding. We also thank the “Commissariat Général aux Investissements” and the “Agence Nationale de la Recherche” for their financial support in the “Programme d’Investissement d’Avenir” (PIA). The French Research Federation Fermat FR3089 is acknowledged for providing TDXRD facility. We are grateful to I. Pasquet (CIRIMAT) and UMS Castaing for FEG-SEM observations.

## REFERENCES

- (1) Morris, J. E. Nanoparticle Properties. In *Nanopackaging*; Morris, J. E., Ed.; Springer: US, 2008; pp 93–107.
- (2) Pawlow, P. Über die Abhängigkeit des Schmelzpunktes von der Oberflächenenergie eines festen Körpers. *Z. Phys. Chem.* **1909**, *65U*, 1–35.
- (3) Takagi, M. Electron-Diffraction Study of Liquid-Solid Transition of Thin Metal Films. *J. Phys. Soc. Jpn.* **1954**, *9*, 359–363.
- (4) Jiang, H.; Moon, K.; Wong, C. P. Recent advances of nanolead-free solder material for low processing temperature interconnect applications. *Microelectron. Reliab.* **2013**, *53*, 1968–1978.
- (5) Kiryukhina, K.; et al. Silver oxalate-based solders: New materials for high thermal conductivity microjoining. *Scr. Mater.* **2013**, *68*, 623–626.
- (6) Kiryukhina, K.; et al. Silver oxalate: towards a new solder material for highly dissipative electronic assemblies. *Int. Symp. Microelectron.* **2013**, *2013*, 000836–000841.
- (7) Abtew, M.; Selvaduray, G. Lead-free Solders in Microelectronics. *Mater. Sci. Eng., R* **2000**, *27*, 95–141.
- (8) *Handbook of lead-free solder technology for microelectronic assemblies*; Marcel Dekker, 2004.

- (9) Kotadia, H. R.; Howes, P. D.; Mannan, S. H. A review: On the development of low melting temperature Pb-free solders. *Microelectron. Reliab.* **2014**, *54*, 1253–1273.
- (10) Cho, J.; Mallampati, S.; Schoeller, H.; Yin, L.; Shaddock, D. In *Developments of Bi-Sb-Cu alloys as a high-temperature Pb-free solder*, Proceedings of the Electronic Components and Technology Conference, San Diego, CA, May 26–29, 2015; IEEE, 2015; pp 1251–1256.
- (11) Menon, S.; George, E.; Osterman, M.; Pecht, M. High lead solder (over 85%) solder in the electronics industry: RoHS exemptions and alternatives. *J. Mater. Sci.: Mater. Electron.* **2015**, *26*, 4021–4030.
- (12) Mallampati, S.; Schoeller, H.; Yin, L.; Shaddock, D.; Cho, J. In *Developments of high-Bi alloys as a high temperature Pb-free solder*, Proceedings of the Electronic Components and Technology Conference, Orlando, FL, May 27–30, 2014; IEEE, 2014; pp 1328–1334.
- (13) Hagberg, J.; Uusimäki, A.; Levoska, J.; Leppävuori, S. Preparation of Bi-Pb-Sr-Ca-Cu-O high T<sub>c</sub> superconducting material via oxalate route at various pH values. *Phys. C* **1989**, *160*, 369–374.
- (14) Marta, L.; Zaharescu, M.; Ciontea, L.; Petrisor, T. Chemical route to the synthesis of superconducting bismuth oxide system. *Appl. Supercond.* **1993**, *1*, 677–691.
- (15) Popa, M.; Țoțovăni, A.; Popescu, L.; Drăgan, N.; Zaharescu, M. Reactivity of the Bi, Sr, Ca, Cu oxalate powders used in BSCCO preparation. *J. Eur. Ceram. Soc.* **1998**, *18*, 1265–1271.
- (16) Villegas, M.; Moure, C.; Fernandez, J. F.; Duran, P. Low-temperature sintering of submicronic randomly oriented Bi<sub>4</sub>Ti<sub>3</sub>O<sub>12</sub> materials. *Ceram. Int.* **1996**, *22*, 15–22.
- (17) Umabala, A.; Suresh, M.; Prasadarao, A. Bismuth titanate from coprecipitated stoichiometric hydroxide precursors. *Mater. Lett.* **2000**, *44*, 175–180.
- (18) Devillers, M.; De Smet, F.; Tirions, O. Bismuth and mixed bismuth-lanthanide carboxylates as precursors for pure and Ln-promoted bismuth molybdate catalysts. *Thermochim. Acta* **1995**, *260*, 165–185.
- (19) Devillers, M.; Tirions, O.; Cadus, L.; Ruiz, P.; Delmon, B. Bismuth Carboxylates as Precursors for the Incorporation of Bismuth in Oxide-based Materials. *J. Solid State Chem.* **1996**, *126*, 152–160.
- (20) Chen, R.; et al. Fabrication of mesh-like bismuth oxide single crystalline nanoflakes and their visible light photocatalytic activity. *J. Alloys Compd.* **2011**, *509*, 2588–2596.
- (21) Muruganandham, M.; et al. Facile Fabrication of Tunable Bi<sub>2</sub>O<sub>3</sub> Self-Assembly and Its Visible Light Photocatalytic Activity. *J. Phys. Chem. C* **2012**, *116*, 12906–12915.
- (22) Wang, H.; Yang, H.; Lu, L. Topochemical synthesis of Bi<sub>2</sub>O<sub>3</sub> microribbons derived from a bismuth oxalate precursor as high-performance lithium-ion batteries. *RSC Adv.* **2014**, *4*, 17483.
- (23) Polla, G.; Baggio, R. F.; Manghi, E.; De Perazzo, P. K. Gel growth and characterization of bismuth oxalate single crystals. *J. Cryst. Growth* **1984**, *67*, 68–74.
- (24) Kolitsch, U. Two bismuth oxalate hydrates and revision of their chemical formulae. *Acta Crystallogr., Sect. C: Cryst. Struct. Commun.* **2003**, *59*, m501–m504.
- (25) Tortet, L.; Monnereau, O.; Roussel, P.; Conflant, P. Synthesis and characterisation of a new hydrated bismuth (III) oxalate: Bi<sub>2</sub>(C<sub>2</sub>O<sub>4</sub>)<sub>3</sub>·6H<sub>2</sub>O. *J. Phys. IV Proc.* **2004**, *118*, 43–50.
- (26) Tortet, L.; Monnereau, O.; conflant, P.; Vacquier, G. Synthesis and characterization of new hydrated bismuth (III) oxalates. *Ann. Chim.* **2007**, *32*, 69–80.
- (27) Peng, Y.; Yu, P.-P.; Chen, Q.-G.; Zhou, H.-Y.; Xu, A.-W. Facile Fabrication of Bi<sub>12</sub>O<sub>17</sub>Br<sub>2</sub>/Bi<sub>24</sub>O<sub>31</sub>Br<sub>10</sub> Type II Heterostructures with High Visible Photocatalytic Activity. *J. Phys. Chem. C* **2015**, *119*, 13032–13040.
- (28) Xiao, K.; et al. Facile synthesis, electronic structure and photocatalytic activity of a novel Bi-based hydroxyl oxalate Bi(C<sub>2</sub>O<sub>4</sub>)-OH. *Inorg. Chem. Commun.* **2015**, *52*, 5–8.
- (29) Xu, J.; Teng, F.; Yao, W.; Zhu, Y. Morphology-dependent photoelectrochemical properties of multi-scale layered Bi(C<sub>2</sub>O<sub>4</sub>)OH. *RSC Adv.* **2016**, *6*, 23537–23549.
- (30) Liu, Z.; Wang, H.; Pan, G.; Niu, J.; Feng, P. Facile synthesis, structure and enhanced photocatalytic activity of novel BiOBr/Bi(C<sub>2</sub>O<sub>4</sub>)OH composite photocatalysts. *J. Colloid Interface Sci.* **2017**, *486*, 8–15.
- (31) Huang, H.; He, Y.; Lin, Z.; Kang, L.; Zhang, Y. Two Novel Bi-Based Borate Photocatalysts: Crystal Structure, Electronic Structure, Photoelectrochemical Properties, and Photocatalytic Activity under Simulated Solar Light Irradiation. *J. Phys. Chem. C* **2013**, *117*, 22986–22994.
- (32) Huang, H.; et al. Bi<sub>2</sub>O<sub>2</sub>(OH)(NO<sub>3</sub>) as a desirable [Bi<sub>2</sub>O<sub>2</sub>]<sup>2+</sup> layered photocatalyst: strong intrinsic polarity, rational band structure and {001} active facets co-beneficial for robust photooxidation capability. *J. Mater. Chem. A* **2015**, *3*, 24547–24556.
- (33) Rivenet, M.; Roussel, P.; Abraham, F. One-dimensional inorganic arrangement in the bismuth oxalate hydroxide Bi(C<sub>2</sub>O<sub>4</sub>)OH. *J. Solid State Chem.* **2008**, *181*, 2586–2590.
- (34) Dollimore, D. The production of metals and alloys by the decomposition of oxysalts. *Thermochim. Acta* **1991**, *177*, 59–75.
- (35) Baco-Carles, V.; Arnal, A.; Poquillon, D.; Tailhades, P. Correlation between the morphology of cobalt oxalate precursors and the microstructure of metal cobalt powders and compacts. *Powder Technol.* **2008**, *185*, 231–238.
- (36) Baco-Carles, V.; Datas, L.; Tailhades, P. Copper Nanoparticles Prepared from Oxalic Precursors. *ISRN Nanotechnol.* **2011**, *2011*, 1–7.
- (37) Lin, Z.; et al. Morphology-controllable synthesis and thermal decomposition of Ag and Ni oxalate for Ag-Ni alloy electrical contact materials. *Mater. Des.* **2016**, *108*, 640–647.
- (38) Dollimore, D.; Griffiths, D. L. Differential thermal analysis study of various oxalates in oxygen and nitrogen. *J. Therm. Anal.* **1970**, *2*, 229–250.
- (39) Dollimore, D.; Griffiths, D. L.; Nicholson, D. 488. The thermal decomposition of oxalates. Part II. Thermogravimetric analysis of various oxalates in air and in nitrogen. *J. Chem. Soc.* **1963**, 2617.
- (40) Monnereau, O. Synthesis of Bi<sub>2</sub>O<sub>3</sub> by controlled transformation rate thermal analysis: a new route for this oxide? *Solid State Ionics* **2003**, *157*, 163–169.
- (41) Scherrer, P. Bestimmung der Größe und der inneren Struktur von Kolloidteilchen mittels Röntgenstrahlen. *Nachrichten Von Ges. Wiss. Zu Gött. Math.-Phys. Kl.* **1918**, 98–100.
- (42) Cullity, B. D.; Stock, S. R. *Elements of X-ray Diffraction*; Prentice-Hall, 2001.
- (43) Diez, E.; et al. Synthesis of bismuth (III) oxide from oxalate: A study by controlled transformation rate thermal analysis (CRTA). *J. Optoelectron Adv. Mater.* **2000**, *2*, 552–556.
- (44) Medernach, J. W.; Snyder, R. L. Powder Diffraction Patterns and Structures of the Bismuth Oxides. *J. Am. Ceram. Soc.* **1978**, *61*, 494–497.
- (45) Harwig, H. A.; Gerards, A. G. The polymorphism of bismuth sesquioxide. *Thermochim. Acta* **1979**, *28*, 121–131.
- (46) Dollimore, D. The thermal decomposition of oxalates. A review. *Thermochim. Acta* **1987**, *117*, 331–363.
- (47) Olson, E. A.; Efremov, M. Y.; Zhang, M.; Zhang, Z.; Allen, L. H. Size-dependent melting of Bi nanoparticles. *J. Appl. Phys.* **2005**, *97*, 034304.
- (48) Limmer, S. J.; Yelton, W. G.; Erickson, K. J.; Medlin, D. L.; Siegal, M. P. Recrystallized Arrays of Bismuth Nanowires with Trigonal Orientation. *Nano Lett.* **2014**, *14*, 1927–1931.
- (49) Meitl, M. A.; Dellinger, T. M.; Braun, P. V. Bismuth–Ceramic Nanocomposites with Unusual Thermal Stability via High-Energy Ball Milling. *Adv. Funct. Mater.* **2003**, *13*, 795–799.
- (50) Hobosyan, M. A.; Yolchinyan, S. A.; Martirosyan, K. S. A novel nano-energetic system based on bismuth hydroxide. *RSC Adv.* **2016**, *6*, 66564–66570.
- (51) Zou, C. D.; Gao, Y. L.; Yang, B.; Zhai, Q. J. Melting and undercooling of bismuth nanocrystals by solvothermal synthesis. *Phys. B* **2009**, *404*, 4045–4050.
- (52) Peppiatt, S. J. The Melting of Small Particles. II. Bismuth. *Proc. R. Soc. London, Ser. A* **1975**, *345*, 401–412.

- (53) Allen, G. L.; Bayles, R. A.; Gile, W. W.; Jesser, W. A. Small particle melting of pure metals. *Thin Solid Films* **1986**, *144*, 297–308.
- (54) Goswami, R.; Chattopadhyay, K. Melting of Bi nanoparticles embedded in a Zn matrix. *Acta Mater.* **2004**, *52*, 5503–5510.
- (55) Pavlovska, A.; Dobrev, D.; Bauer, E. Surface melting versus surface non-melting: an equilibrium shape study. *Surf. Sci.* **1993**, *286*, 176–181.
- (56) Goswami, R.; Chattopadhyay, K. Depression of melting point of multidomained bismuth in aluminum based metallic glass nanocomposites. *Appl. Phys. Lett.* **1996**, *69*, 910–912.
- (57) Liu, M.; Wang, R. Y. Size-Dependent Melting Behavior of Colloidal In, Sn, and Bi Nanocrystals. *Sci. Rep.* **5**, **2015**.
- (58) Shi, F. G. Size dependent thermal vibrations and melting in nanocrystals. *J. Mater. Res.* **1994**, *9*, 1307–1314.

## Supporting Information

### **Bi<sub>2</sub>(C<sub>2</sub>O<sub>4</sub>)<sub>3</sub>·7H<sub>2</sub>O and Bi(C<sub>2</sub>O<sub>4</sub>)OH Oxalates Thermal Decomposition Revisited.**

#### **Formation of Nanoparticles with a Lower Melting Point than Bulk Bismuth**

*Pierre Roumanille<sup>1,2\*</sup>, Valérie Baco-Carles<sup>2</sup>, Corine Bonningue<sup>2</sup>, Michel Gougeon<sup>2</sup>, Benjamin Duployer<sup>2</sup>, Philippe Monfraix<sup>1</sup>, Hoa Le Trong<sup>1</sup>, Philippe Tailhades<sup>2</sup>*

<sup>1</sup>Institut de Recherche Technologique (IRT) Saint Exupéry, 118 route de Narbonne, CS 44248, 31432 Toulouse Cedex 4, France

<sup>2</sup>Institut Carnot Chimie Balard Cirimat, UMR CNRS 5085, Université de Toulouse, CNRS, INPT, UPS, Université Toulouse 3 Paul Sabatier, 118 route de Narbonne, 31062 Toulouse Cedex 9, France

## **Contents**

$\alpha$ , $\beta$ and $\delta$ -Bi <sub>2</sub> O <sub>3</sub> XRD patterns	Fig. S1-S2
DTA cooling data in air and nitrogen	Fig. S3-S4
TDXRD cooling data in nitrogen	Fig. S5-S6

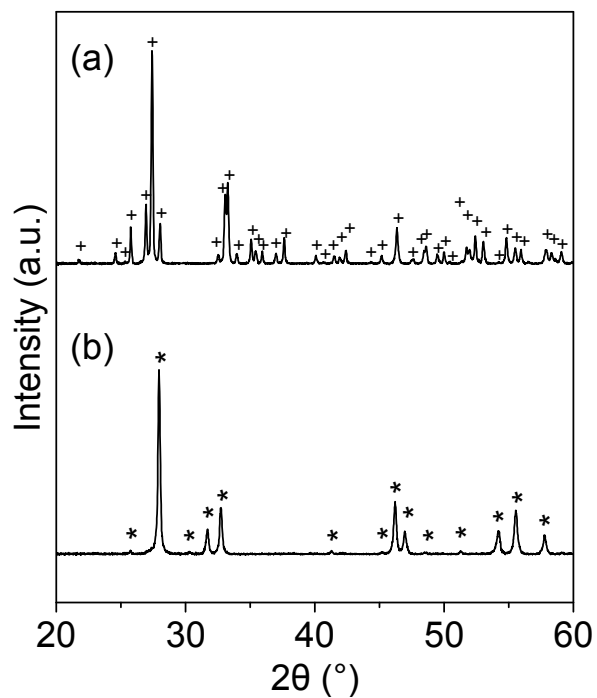


**Figure S1.** XRD patterns of bismuth oxide products obtained from bismuth oxalate decomposition: samples treated at 400°C, (†)  $\alpha$ - $\text{Bi}_2\text{O}_3$ , JCPDS 70-8243 (a); samples treated at 350°C, (\*)  $\beta$ - $\text{Bi}_2\text{O}_3$ , JCPDS 27-0050 (b)

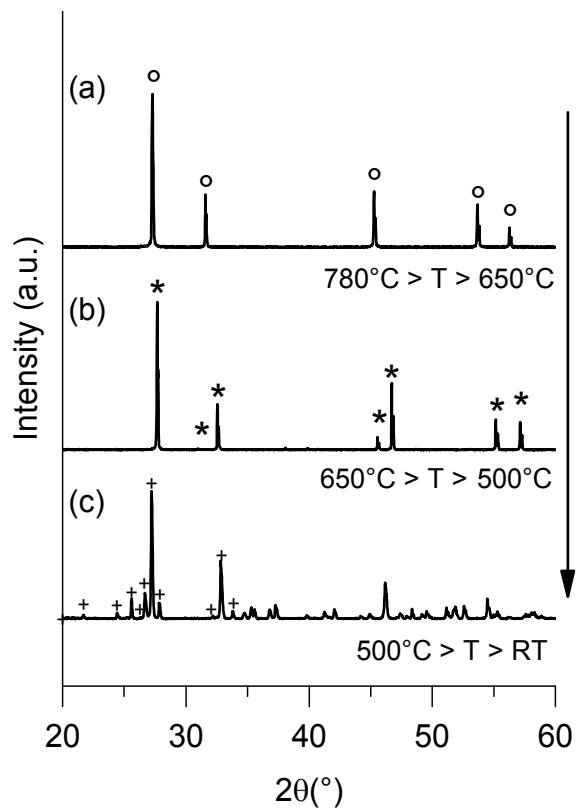


**Figure S2.** TDXRD pattern for bismuth oxalate in air - cooling part :  $\delta$ - $\text{Bi}_2\text{O}_3$ , (°) JCPDS 74-1633 (a) ;  $\beta$ - $\text{Bi}_2\text{O}_3$ , (\*) JCPDS 27-0050 (b) ;  $\alpha$ - $\text{Bi}_2\text{O}_3$ , (†) JCPDS 70-8243 (c)

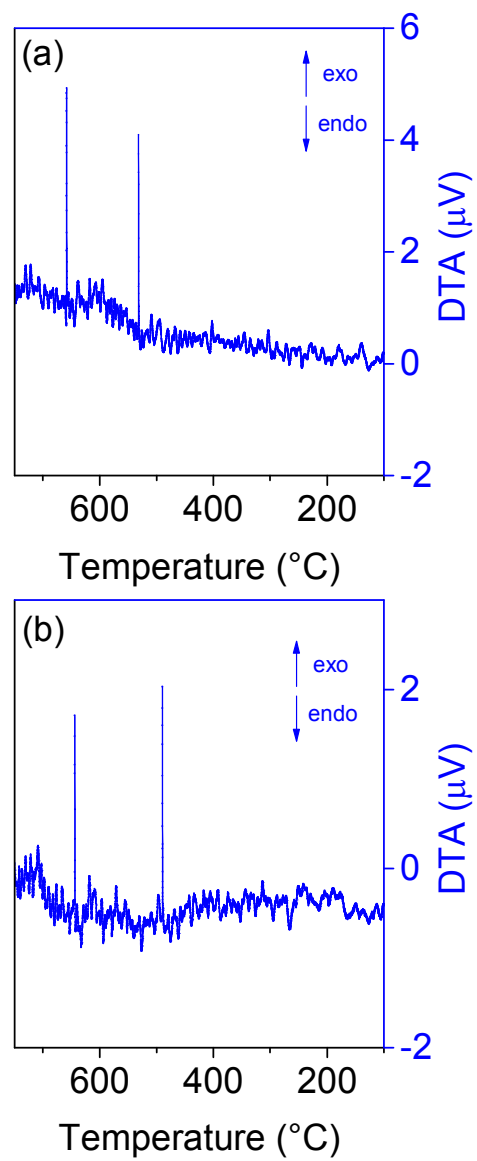


**Figure S3.** DTA data for cooling in air: OxBi(1) (a) ; OxBi(2) (b)

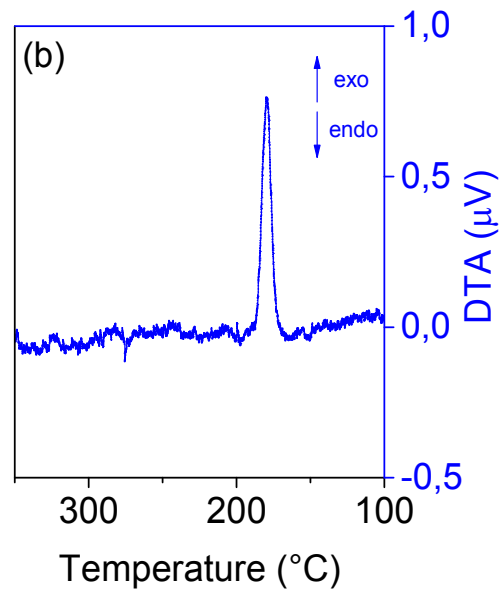
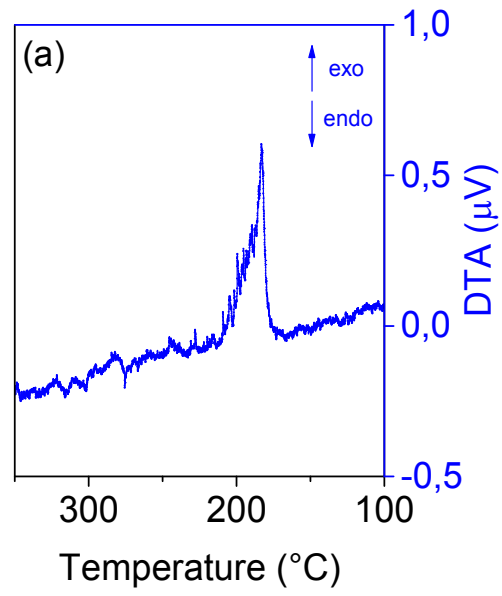


**Figure S4.** DTA data for cooling in nitrogen: OxBi(1) (a) ; OxBi(2) (b)

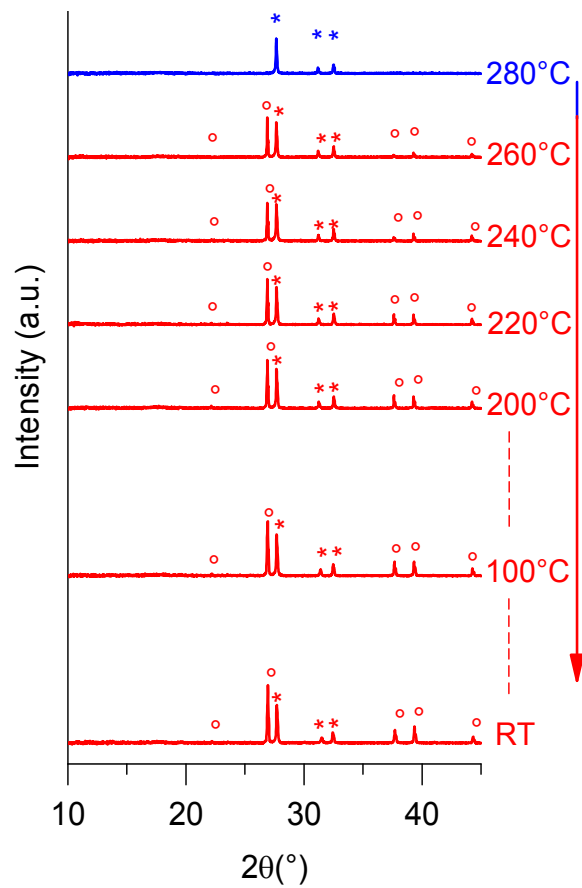


**Figure S5.** TD-XRD pattern for OxBi(1) in nitrogen – cooling part. (°) Bi, JCPDS 85-1329 ; (\*)  $\beta$ - $\text{Bi}_2\text{O}_3$ , JCPDS 27-0050

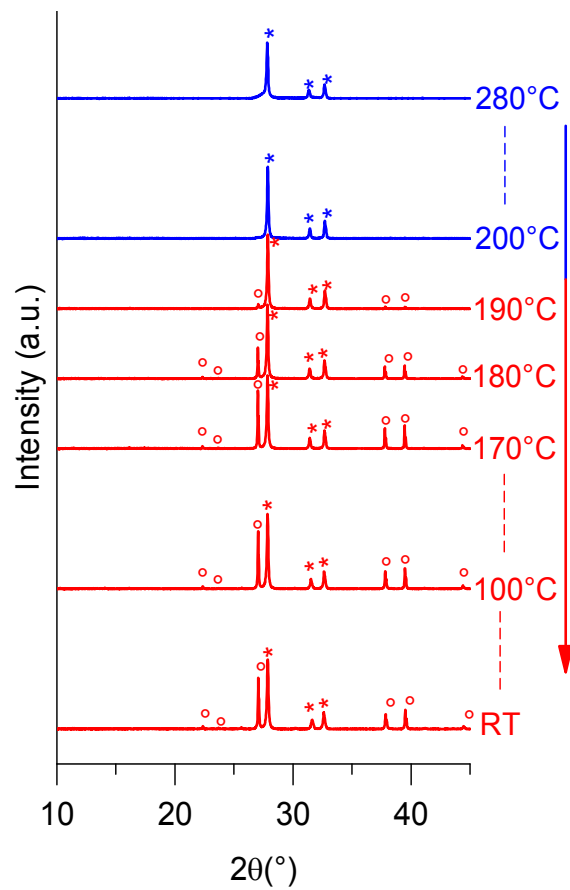


**Figure S6.** TDXRD pattern for OxBi(2) in nitrogen – cooling part, (°) Bi, JCPDS 85-1329 ; (\*)  $\beta$ -Bi<sub>2</sub>O<sub>3</sub>, JCPDS 27-0050